Multinucleated giant cells in human pancreatic cancer are a distinct macrophage population undergoing a DNA damage response and associated with an aggressive tumor microenvironment

Marika Viatore[1,2*], Rebecca Polidori[1,2*], Anna Rita Putignano[2*], Arturo Bonometti[3,4], Daoud Rahal[3], Marialuisa Barbagallo[2], Lisa Veghini[5], Greta Donisi[4,6], Gianluca Basso[7], Desirée Giuliano[7], Sergio Marchini[7], Marco Erreni[4,8], Maria Rita Fumagalli[8], Fabio Pasqualini[2,4], Fabio Grizzi[2], Paola Spaggiari[3], Silvia Uccella[3,4], Silvia Bozzarelli[9], Alessandro Zerbi[4,6], Giovanni Luigi Capretti[4,6], Vincenzo Corbo[5], Massimo Locati[1,2], Alberto Mantovani[2,10], Federica Marchesi[1#]

[1]Department of Medical Biotechnology and Translational Medicine, University of Milan; Milan, Italy;
[2]Department of Immunology and Inflammation, IRCCS Humanitas Research Hospital, Rozzano, Milan, Italy;
[3]Department of Pathology, IRCCS Humanitas Research Hospital, Rozzano, Milan, Italy;
[4]Department of Biomedical Science, Humanitas University, Pieve Emanuele, Milan, Italy;
[5]Department of Engineering for Innovation Medicine, University of Verona, Verona, Italy;
[6]Pancreatic Surgery, IRCCS Humanitas Research Hospital, Rozzano, Milan, Italy;
[7]Humanitas Genomic Facility, IRCCS Humanitas Research Hospital, Rozzano, Milan, Italy;
[8]Unit of Advanced Optical Microscopy, IRCCS Humanitas Research Hospital, Rozzano, Milan, Italy;
[9]Medical Oncology and Hematology Unit, Humanitas Cancer Center, IRCCS Humanitas Research Hospital, Milan, Italy;
[10]The William Harvey Research Institute, Queen Mary University of London, London, UK.

[*]These authors contributed equally to this work.

[#]Correspondence to Federica Marchesi, PhD; Department of Medical Biotechnology and Translational Medicine, University of Milan, Via Fratelli Cervi, 93 - L.I.T.A. 20054 Segrate (MI); Email: federica.marchesi@unimi.it

Running title: Multinucleated macrophages in human pancreatic cancer

Conflict of interest: The authors declare no potential conflicts of interest.

Funding information: This work was supported by Associazione Italiana per la ricerca sul cancro (AIRC) under grant AIRC IG 2025 - ID. 31899 (to FM) and by the project "SCALE UP – Department of Excellence 2023-2027", funded by the Italian Ministry of University and Research to the Department of Molecular Biotechnology and Translational Medicine". The PhD students Marika Viatore and Rebecca Polidori were supported by the PhD program in Experimental Medicine of the University of Milan and by an AIRC fellowship for Italy. The funding agencies had no role in design of the study, collection and analysis of data.

Abstract

Macrophages constitute a dominant and functionally diverse immune population within the microenvironment of pancreatic ductal adenocarcinoma (PDAC), yet how macrophage heterogeneity contributes to the tumor remains poorly defined. In an institutional cohort of 145 PDAC specimens, we identified a population of multinucleated giant cells (MGCs) of macrophage origin, an entity previously described in chronic inflammation but rarely in cancer. $CD68^+$ MGCs were present in 28% of tumors, enriched in squamous, non-glandular regions, and more frequent after neoadjuvant chemotherapy. By integrating spatial transcriptomics and quantitative imaging, we defined the features of these cells, which, compared with MGCs in non-neoplastic inflammatory lesions, lacked canonical polarization markers (HLA-DR, CD163) and displayed a distinctive transcriptional program characterized by upregulation of the *POLR2K*, *TUBA8*, *COX5B*, and *VDAC1* genes, which encode proteins involved in DNA repair, oxidative stress, and MYC signaling. Spatial analyses revealed activation of hypoxia and extracellular matrix–remodeling pathways in MGC-associated niches, and experimental hypoxia promoted MGC formation *in vitro*. Consistent with these data, we found that in the TCGA PAAD dataset a macrophage MGC gene signature was enriched in the squamous PDAC subtype and correlated with poorer overall survival ($p = 0.018$). Morphometric and immunofluorescence analyses further showed increased $53BP1^+Ki67^+$ nuclei and nuclear atypia in MGCs, indicating ongoing proliferation despite DNA damage. Together, these data identify MGCs of macrophage origin as an immune cell state shaped by hypoxia and stress signaling, associated with aggressive tumor phenotypes, and potentially exploitable as an immune classifier in PDAC.

Synopsis

Macrophages in the PDAC microenvironment are heterogenous. The authors identify a previously unrecognized population of stress-induced, multinucleated macrophages. The cells are driven by hypoxia and DNA damage and associated with poor prognosis, suggesting novel classifiers for patient stratification.

Introduction

Multinucleated giant cells (MGCs) are a morphological subtype of polyploid macrophages documented in non-malignant, chronically inflamed tissues, including the lung of patients with tuberculosis, in sarcoidosis, in chronic granulomatous disease (CGD) and in lesions associated with foreign body immune responses (1-3). Recently, their presence has also been reported in cancerous tissues (4-6). The mechanisms underlying the formation and functional role of MGCs within pathological contexts remain poorly understood, suggesting that their contribution to disease progression or resolution may differ depending on the stimulus that has triggered their polyploidy. *In vitro*, multinucleated macrophages can be obtained by prolonged stimulation with different cytokines (2, 7). Specifically, IFNγ drives *in vitro* macrophages towards a phenotype resembling Langhans cells, i.e. multinucleated macrophages associated with granulomas in tuberculosis; IL-4 stimulation induces macrophages with features of foreign-body giant cells, a hallmark of inflammatory responses to inert materials such as talc, suture, or medical implants; and receptor activator of nuclear factor kappa-B ligand (RANKL) drives macrophages towards a phenotype resembling osteoclasts, bone-resorbing multinucleated macrophages found in homeostatic conditions in the bone (7). Morphological differences of MGCs, especially related to the nuclear spatial arrangement, are retained *in vivo*, in different pathological contexts (2, 3). Langhans cells exhibit a characteristic horseshoe-shaped arrangement of nuclei along the cell periphery (2, 8), foreign-body giant cells display numerous nuclei irregularly distributed within the cytoplasm (2, 3), Touton giant cells feature a circular arrangement of nuclei and foamy cytoplasm at the cell periphery, while osteoclasts have apical and evenly distributed nuclei (2). Relatively little is known about the nuclear patterns characterizing MGCs in tumor tissues.

Pancreatic ductal adenocarcinoma (PDAC) is marked by a heterogeneous immune landscape and a dense desmoplastic reaction, which collectively drive tumor progression and therapeutic resistance (9, 10). Among immune populations, macrophages represent a major component of the PDAC microenvironment, and their diverse phenotypes have been linked to variable patient outcomes and treatment responses (11-14). Defining macrophage-based classifiers may therefore refine therapeutic stratification and better capture PDAC clinical heterogeneity. Beyond density and spatial distribution, recent studies, including our own (15), have highlighted the importance of macrophage morphology in human cancers. The results have shown that morphological metrics can distinguish macrophage subsets, reflect functional

states, and predict clinical outcomes in human tumors (15, 16). Herein, we report that while investigating the morphology of tumor-associate macrophages (TAM) in human PDAC, we came across a population of macrophages with features of MGCs. Understanding the specific functions of these cells and whether their presence in the tumor microenvironment is beneficial or detrimental is of particular importance.

Overall, the functional role of MGCs remains an open question. Langhans cells emerging during infectious diseases are hypothesized to contribute to the eradication of persistent bacteria. Nonetheless, studies have not demonstrated increased phagocytosis or microbial killing by these cells (3). In the specific context of *Mycobacterium tuberculosis* infection, Langhans cells have been shown to express high levels of antigen-presenting molecules and play a role in preventing pathogen dissemination. Foreign-body giant cells form in response to indigestible material (17); however, experimental findings have yielded conflicting results, with reports of enhanced, unchanged, or even diminished phagocytic activity compared to their mononucleated macrophage counterparts (18).

With these premises, here we investigated the occurrence of MGCs in human pancreatic cancer, their morphological features, and their functional profile in comparison with MGCs commonly associated to non-neoplastic inflammatory conditions. The results reported here support the hypothesis that MGCs in PDAC are stress-induced, DNA damage–responsive cells, preferentially localized in squamous tumor regions and associated with an aggressive tumor microenvironment.

Materials and Methods

Patients and study population

The study population included 145 samples from PDAC patients (**Supplementary Table S1**), aged older than 18 years, who had undergone pancreatic resection between 2010 and 2018 at Humanitas Research Hospital. All patients provided written informed consent, and the study was conducted in accordance with the Declaration of Helsinki and approved by the Institutional Ethical Committee (protocol number n° 595 and 979/20). The number of MGCs was manually evaluated by two independent expert pathologists (A.B. and R.D.) on formalin-fixed, paraffin-embedded (FFPE) tissue sections that had been previously stained with a CD68 antibody (12). The two expert pathologists also reviewed all the slides to exclude the presence of giant cell tumors of soft tissue (19) or undifferentiated carcinoma with osteoclast-like giant cells (20). When specified, 4 samples from lungs with tuberculosis (ProteoGenex, CA), and 4 samples from skin lesions undergoing secondary intention healing (from the archive of the Pathology Department at Humanitas) were also analyzed.

Immunohistochemistry (IHC) staining

After deparaffinization and rehydration, antigen retrieval was performed by heat treatment in a water bath at 98°C for 20 min. Details related to each antibody used are summarized in **Supplementary Table S2**. Endogenous peroxidases were blocked with hydrogen peroxide 3% (Perhydrol ® Merck) for 10 min at room temperature (RT). Nonspecific binding block was performed with Background Sniper (Biocare Medical) for 10 min at RT. Sections were incubated with the primary antibodies according to the conditions listed in **Supplementary Table S2**, washed, and then incubated with the MACH 1 Universal Polymer Detection system (Biocare Medical). Diaminobenzidine tetrahydrochloride (Biocare Medical) was used as a chromogen to visualize the positive cells. Nuclei were lightly counterstained with a Hematoxylin solution (Histo-Line). Sections were dehydrated and mounted with a mounting medium (Eukitt). Tissue slides were digitally acquired by the ZEISS Axio Scan Z1 Slide Scanner at a magnification of 20x. The integrity of the tissue sections was thoroughly examined prior to further analysis.

Picrosirius red staining

PDAC FFPE tissue sections (4 μm thick) were deparaffinized in xylene and rehydrated through a graded ethanol series. Sections were stained with Weigert's iron hematoxylin (1:1, solution

A:solution B) (Electron Microscopy Sciences 26102-1A and 26102-1B) for 8 minutes and rinsed in running tap water for 10 minutes. Slides were then incubated for 1 hour at room temperature in Picro-Sirius Red solution (0.5 g Direct Red 80 (Sigma #365548) in 500 ml of saturated picric acid) and washed twice with acidified water. After dehydration through graded ethanol, slides were mounted using Eukitt mounting medium (Sigma-Aldrich). Whole-slide images were captured with a ZEISS Axio Scan.Z1 slide scanner at 20× magnification. For each whole slide, the area covered by fibrosis within the tumor annotation was quantified by a pixel classifier in QuPath, detecting picrosirius red^{+} collagen fibers.

Immunofluorescence (IF) staining

The initial steps for deparaffinization, rehydration, and antigen retrieval were performed as described for IHC, using AR9 buffer (Akoya Biosciences) for all heat-induced retrieval steps. Following blocking with the reagent provided in the Opal Multiplex IHC kit (RRID:AB_3665660), tissue sections were incubated with primary antibodies (**Supplementary Table S2**) and subsequently with HRP-conjugated secondary antibodies from the Opal Multiplex IHC kit. Fluorescent signal detection was carried out using Opal fluorophores (**Supplementary Table S2**), and antibody removal between rounds was achieved via iterative heat-mediated stripping in AR9 buffer. Nuclei were counterstained with DAPI for 5 minutes at RT. Slides were mounted with Agilent Fluorescence Mounting Medium (S302380-2, Agilent), coverslipped, and digitally scanned using the ZEISS Axio Scan Z1 Slide Scanner (RRID:SCR_020927) at 20× magnification. Staining of PDAC sections with anti-53BP1 and anti-Ki67 was performed on 3 slides. 20,000 positive nuclei were analyzed using QuPath (RRID:SCR_018257, version 0.5.1), by annotating nuclei within approximately 240 MGCs and 4,000 macrophages, identified based on CD68 expression and morphological criteria. For each annotated nucleus, the expression of 53BP1 and Ki67 was assessed, and the proportion of nuclei positive for each marker individually or co-expressing both was quantified.

Stimulated Emission Depletion (*STED) Microscopy Image Acquisition and Processing*

PDAC tissue sections were stained by IF with anti-CD68 (RRDI: AB_2314148, M0814, Dako) and anti-Lamin B1 (RRID: AB_443298, ab16048, Abcam) antibodies, as described above, and then analyzed by STED microscopy. STED microscopy xyz images were acquired with a Leica SP8 STED3X confocal microscope, using a Leica HC PL APO 100x/1.40 oil STED White Objective. Opal 570 and Opal 650 were excited with a 627 nm and 550 nm tuned White Light

Laser (WLL), respectively. Fluorescence emission was collected from 554 nm to 603 nm for Opal 570 and from 631 nm to 720 nm for Opal 650. Gated 775 nm-pulsed STED laser was applied. Emission filter bandwidths and sequential scanning acquisition were set up to avoid spectral overlap between fluorophores. Deconvolution was applied to STED images using Huygens Professional software (version 24.10). Images were finally processed with Imaris software (RRID:SCR_007370, version 9.7.2) (Bitplane).

Hematoxylin and eosin (H&E) staining

Four-micron-thick formalin-fixed paraffin-embedded (FFPE) sections consecutive to those used for IHC were deparaffinized in xylene and rehydrated through a graded alcohol series. Tissue sections were stained with hematoxylin (Histo-Line) for 10 minutes and eosin (Histo-Line) for 7 minutes, dehydrated through graded alcohols, and mounted with Eukitt (Sigma-Aldrich). Whole-slide digital images were acquired using a ZEISS Axio Scan Z1 Slide Scanner at 20X magnification.

Histological assessment of PDAC morphotypes

30 circular regions of interest (ROIs) (diameter=1000 μm) containing MGCs were outlined on H&E slides from 15 PDAC samples. ROIs were classified as either glandular or non-glandular (21) by an expert pathologist based on tumor morphology.

Cellular and nuclear metrics

Morphological properties of MGCs (i.e. cell size, number of nuclei, nuclear circularity index, spread index and average distance of the nuclei to the membrane) were calculated using QuPath (version 0.5.1), by randomly selecting 60 MGCs per disease, from three different H&E-stained slides. MGC contours were manually annotated and cell size automatically computed by the QuPath's function *Add shape features*. Nuclei were detected and segmented by Stardist (version 0.5.0) and nuclear indices were calculated based on the coordinates of the nuclei centroids and the centroid of the corresponding MGC. Circularity Index (uniformity of the nuclei distribution around the cell centroid) was defined as: $C = \frac{1}{N}\sum_{i=1}^{N}\left(\frac{d_i}{r}\right)^2$, where d_i represents the distance of each nucleus to the cell centroid and r is the cell radius. Spread Index (how dispersed the nuclei are around the cell centroid) is defined as: $S = \frac{Var(d_i)}{r^2}$, where $Var(d_i)$ represents the variance of the distances of nuclei from the cell centroid, and r^2 is proportional

to the cell area. The mean distance of the nuclei to the membrane is computed automatically by using the QuPath's function *Signed distance to membrane*.

Imaging mass cytometry (IMC) staining

FFPE tissue sections from pancreatic cancer (n=3), tuberculosis (n=3), or skin lesions (n=3) were deparaffinized using xylene and rehydrated through a graded alcohol series. Antigen retrieval was performed by heating the sections in a water bath at 98°C for 20 minutes in Target Retrieval Solution, pH 9 (S1699, Agilent), followed by cooling in distilled water. After blocking, slides were incubated overnight at 4°C with the Human Immuno-Oncology IMC Panel, 31 Antibodies (201509, Standard BioTools), followed by two washes for 8 minutes each in 0.2% Triton X-100 (Sigma) $PBS^{+/+}$ and then two washes for 8 minutes each in $PBS^{+/+}$. Finally, the sections were incubated with 0.63 µg/mL Cell-ID Intercalator-Ir (Standard BioTools) (22). 3 ROIs without MGCs and 5 ROIs with MGCs were selected per sample.

IMC analysis

IMC images were preprocessed and normalized using the custom R pipeline described in (23), which includes a cell segmentation step performed by Ilastik (RRID:SCR_015246, version 1.4.0) and CellProfiler Image Analysis Software (RRID:SCR_007358, version 4.2.6). Subsequent unsupervised clustering and cell phenotyping were performed following the pipeline described in (22), which incorporated the use of QuPath for visualization and cell measurement extraction, and CytoMAP (RRID:SCR_021227) for unsupervised clustering. Macrophages were identified by clusters of $CD68^{+}$ and $CD163^{+}$ cells, while MGCs were retrospectively annotated starting from these two clusters. Due to limitations of the Ilastik segmentation algorithm in recognizing shared cytoplasmic boundaries, MGCs were not automatically classified as single entities. Post-processing in QuPath was therefore performed to manually merge adjacent mononuclear macrophage annotations into unified multinucleated giant cells.

Spatial transcriptomics

Spatial transcriptomics was performed using the GeoMx® Digital Spatial Profiler (Nanostring) platform (RRID:SCR_021660). For each pathology (tuberculosis, skin lesion and PDAC), we analyzed up to 37 regions of interest (ROIs) from n=4 slides (one slide per patient). After deparaffinization and target retrieval, slides were incubated with 0.1 µg/mL proteinase K (25530049, Invitrogen™) for 15 minutes at 37°C and then post fixed for 5 minutes in 10%

neutral buffered formalin followed by two washes in NBF stop buffer (24.5 g Tris base and 15 g Glycine in 2 L DEPC water). Slides were incubated with the Whole Transcriptome Atlas (WTA) RNA Probe set (121401102, NanoString), according to the manufacturer's protocol. Following probe incubation, slides were washed and incubated with the morphology marker solution: AlexaFluor™ 647 anti-human CD68 (BL13756, 375606 BioLegend, 1:400, RRID:AB_3097193) plus SYTO 13 (provided in GeoMx Nuclear Stain Morphology Kit, 121300303, NanoString) for 1 hour at RT and processed through the GeoMx® Digital Spatial Profiler instrument. ROIs with a circular shape and a diameter of 600 μm were selected, with an average of 3 ROIs without MGCs and 5 ROIs with MGCs per patient. For each ROI, the $CD68^+$ area of interest (AOI) was selected to collect barcodes in a 96-well plate. Barcoded oligonucleotides (GMX-RNA-NGS-HUWTA-4, Bruker Spatial Biology) were prepared for Illumina-based sequencing to generate target probe–specific count files, which were then saved in a digital count conversion (.dcc) format.

DSP data analysis

NanoString GeoMx Digital Spatial Profiling (DSP) libraries were sequenced on an Illumina Nextseq2000, and files in BCL format were converted to FASTQ using *BCLconvert* (version 3.8.2). For each AOI, .dcc files were generated from fastqs using the GeoMx NGS Pipeline (version 3.1.1). From each tissue under investigation .dcc files were read into a NanoStringGeoMxSet object using the *readNanoStringGeoMxSet* function from *GeomxTools* R package (version 3.5, R version 4.3.3), and segments were assessed for sequence quality. After generating gene-level counts, segments with high fraction of genes detected below the limit of quantification (LOQ) were removed. Count matrix, sample annotations, and feature annotations were read into a SpatialExperiment object and analyzed with *standR* package (version 1.6) workflow. Genes with low expression levels were removed. Counts were normalized using the upper-quartile method from the *edgeR* package (version 4.0.16). Principal component analysis (PCA) was used to detect unwanted variation due to slide effect. Batch effect correction was performed with RUV4 (Removal of Unwanted Variation 4). The limma-voom pipeline was used to identify differentially expressed genes among multinucleated and mononucleated macrophages. Pre-ranked Gene set enrichment analysis (GSEA) was performed with *fgsea* R package (version 1.28) using MSigDB genesets (Hallmark, Reactome, Gene Ontology Biological Process).

Fluorescence in situ hybridization (FISH)

DNA-FISH was performed on FFPE PDAC tissue sections using the Vysis® LSI® MYC Dual Color, Break Apart Rearrangement Probe (Abbott Molecular), according to the manufacturer's instructions. Briefly, after deparaffinization and pretreatment, tissue sections were hybridized with the probe and incubated overnight at RT. Following post-hybridization washes, nuclei were counterstained with DAPI. Slides were imaged using the LEICA DM5500 B microscope at 1000x magnification, and MYC signals were quantified using QuPath software. Fluorescence images were acquired and analyzed using QuPath software. Nuclei were identified based on DAPI staining, and MGCs were distinguished from mononuclear macrophages based on the presence of multiple closely adjacent nuclei. MYC signals were detected using a pixel classifier to identify fluorescent dots, which were automatically quantified and normalized to the number of nuclei. This approach allowed us to exclude that differences in MYC signal were merely due to multinucleation, indicating instead an increased MYC gene copy number per nucleus in these cells.

In vitro differentiation of human MGCs

Human peripheral blood mononuclear cells (PBMCs) were obtained from buffy coat fractions of healthy donors in accordance with the protocol approved by the Institutional Review Board (IRB) of Humanitas Research Hospital (approval 28/01/2016), by density-gradient centrifugation using Ficoll®. Monocytes were isolated using Pan Monocyte Isolation Kit, human (Miltenyi Biotec, 130-096-537) and plated at a density of 3×10^6 cells per well in 6-well plates. Cells were cultured in RPMI (ECB9006L, Euroclone) supplemented with 10% heat-inactivated fetal bovine serum (FBS) (97068-085, VWR), 1% penicillin–streptomycin (ECB3001D, Euroclone), and 1% L-glutamine (BCP04-80100, Bio-cell), together with 50 ng/mL macrophage colony-stimulating factor (M-CSF) (130-096-492, Miltenyi) for 5 days to promote differentiation into macrophages. On day 6, one 6-well plate was transferred to a hypoxia incubator set at 3% O_2 for 48 h, while the second plate remained under normoxia. After 48 h, both plates were returned to the normoxic incubator, and cells were maintained for 4 weeks in standard culture conditions. On day 28 after hypoxia exposure, cells were fixed and stained using the Diff-Quik kit (04-090805M, Bio Optica) according to the manufacturer's instructions. Each solution was applied for 1 min, followed by two rapid washes in distilled water. Slides were air-dried before imaging. Images were acquired at 20× magnification using an Olympus IX53 microscope. Cell quantification was performed using QuPath software (version 6.0). Cells were automatically detected by applying a hematoxylin-based threshold to identify individual nuclei, generating one object per cell and allowing estimation of the total

number of cells per image. MGCs were manually identified and counted in each image. To assess the role of MYC signaling in hypoxia-induced multinucleation, macrophages were treated with the MYC inhibitor 10058-F4 (25 μM; Sigma Aldrich) during hypoxic exposure (3% O_2). In parallel, to assess the direct effect of chemotherapeutic agents on macrophage multinucleation, macrophages were treated with gemcitabine (GEM; 500 nM and 750 nM; S1714) or paclitaxel (PTX; 500 nM and 750 nM; S1150). Treatments were performed for 3 weeks, followed by 1 additional week in standard culture conditions prior to fixation (total culture time of 4 weeks). Two wells per condition were included in each experiment, and three independent experiments were performed. Control cells received an equivalent volume of vehicle (DMSO) throughout all experiments. The frequency of MGCs was then compared across conditions.

Single-cell RNA-sequencing dataset and analysis

The Steele et al. human PDAC single-cell RNA-sequencing dataset was downloaded from the GEO database under accession number GSE155698 and used to refine the MGC signature. In our re-analysis, the final Seurat object included 16 PDAC tissue samples and 35,180 cells after quality-control filtering and downstream processing. Filtered feature-barcode matrices were loaded into R and analyzed using the Seurat package version 4.4.0. Cells expressing at least 200 genes were retained, and genes expressed in at least 3 cells were included in the analysis. Additional quality-control filtering was performed for each sample to remove low-quality cells based on median absolute deviation from the distribution of transcripts per cell, as well as the percentage of mitochondrial and ribosomal gene expression. Data were normalized using the log-normalization method implemented in the NormalizeData function with default parameters. The 2,000 most variable genes shared across datasets were selected, and datasets were integrated using Harmony version 1.2.0, with dataset identity used as the grouping variable. The number of principal components used to construct the shared nearest neighbor graph was selected based on elbow plot inspection. Cells were clustered using the Louvain algorithm implemented in the FindClusters function. Cell types were annotated based on cluster-specific marker genes identified using the MAST method implemented in FindMarkers, with dataset included as a latent variable to account for batch effects.

MGC gene signature in PDAC

Leading-edge genes from selected pathways enriched in MGCs-containing ROIs compared to mononucleated Mϕ ROIs in the in-house GeoMx DSP dataset were used as candidate genes to construct a MGC gene signature. To reduce potential contamination from tumor-derived gene expression, the candidate gene list was refined using the independently re-analyzed Steele et al. PDAC single-cell RNA-sequencing dataset described above. Specifically, candidate genes highly expressed in malignant epithelial/tumor cell clusters were excluded, whereas genes enriched in tumor-associated macrophage clusters were retained. Thus, the final MGC signature was derived from our GeoMX PDAC leading-edge analysis and refined using malignant epithelial and tumor-associated macrophage annotations from the independent PDAC single-cell RNA-sequencing reference dataset.

TCGA survival analysis

Gene expression profiles and corresponding clinical data from primary TCGA PDAC patients (PAAD dataset, n=170) were obtained from the Genomic Data Commons (GDC) Data Portal via the R package *TCGAbiolinks* (version 2.25.3, R version 4.1.1). Data retrieval was performed with the *GDCquery* function with the following parameters: project = "TCGA-PAAD", data.category = "Transcriptome Profiling", data.type = "Gene Expression Quantification", experimental.strategy = "RNA-Seq", and workflow.type = "STAR – Counts". Count data were then processed using the *DESeq2* package (version 1.34), and variance-stabilized expression values were used for Gene set variation analysis (GSVA) to evaluate the enrichment of the defined MGC signature across samples (24). GSVA was performed using *gsva* function with parameters: kcdf = "Gaussian", mx.diff = TRUE, method = 'gsva'. For survival analysis, patients were stratified using a predefined cutoff based on the median absolute deviation ± 5% (MAD) of the MGC GSVA score, excluding samples with intermediate scores and minimizing potential bias introduced by optimized cutpoint selection. Overall survival was analyzed using Kaplan-Meier curves, and differences between groups were assessed using the log-rank Mantel-Cox test. Survival analyses were performed using the *survival* (version 3.4) and *survminer* (version 0.4.9) R packages.

Molecular profiling

To classify PDAC samples from The Cancer Genome Atlas (TCGA-PAAD) into molecular subtypes, we applied the Moffitt et al. classification scheme based on transcriptomic signatures (25). Log-transformed TPM (Transcripts Per Million) expression data were obtained using the

R/Bioconductor package *TCGAbiolinks* and processed using the GSVA algorithm to compute enrichment scores for the "classical" and "basal-like" (squamous) gene signatures defined by Moffitt et al. (25). Each sample was assigned to the "Classical" subtype if its GSVA score for the classical signature was higher than for the squamous signature, and to the "Squamous" subtype if the reverse was true. MGC signature GSVA scores were compared between Classical and Squamous tumors using a two-sided Mann–Whitney test.

RNA extraction from FFPE tissue sections

Consecutive slides of FFPE tissue samples (3-4/sample) were obtained from selected PDAC patients who had received or not neoadjuvant chemotherapy. Tumor area was scraped from each slide and collected into a vial, then RNA purification was performed using the NucleoSpin® totalRNA FFPE XS kit (Macherey-Nagel), following the manufacturer's instruction. Total RNA from each sample was then purified using the NucleoSpin® RNA Clean-up XS kit (Macherey-Nagel), according to the manufacturer's instruction.

RNA sequencing analysis

Libraries were prepared from RNA extracted from FFPE tissue sections using the SMARTer® Stranded Total RNA-seq Kit v3 Pico Input Mammalian (Takara Bio), following the manufacturer's instructions. Paired-end sequencing (2x76 bp) was carried out on an Illumina Nextseq 550 platform, yielding an average of ~60 million reads per sample. Raw sequencing data were processed using Cogent NGS Analysis Pipeline (CogentAP, version 3.1) from Takara Bio, optimized for SMARTer RNA-seq libraries. CogentAP pipeline integrates multiple tools for quality control, alignment, and quantification. Briefly, BCL files were demultiplexed into FASTQ files using bcl2fastq (version 2.20.0) with a Cogent-formatted sample sheet. Barcode and Unique Molecular Identifier (UMI) were extracted from the reads and encoded into the read names. Adapter trimming was performed using Cutadapt to remove residual adapter sequences. Trimmed reads were aligned to the human reference genome (GRCh38/hg38) using the STAR aligner. SortMeRNA was employed to filter out rRNA reads prior to quantification. Deduplication was performed using UMI sequences to identify and remove PCR duplicates (UMI-tools). Gene- and transcript-level quantification was carried out using Salmon. Transcript-level quantifications generated by Salmon were imported and summarized to the gene level using the *tximport* R package (version 1.30, R version 4.3.3). The resulting gene-level count matrix was then used as input for downstream analyses with the

edgeR package (version 4.0.16). Low counts genes were filtered using filterByExpr function, and library size normalization was performed using the TMM (Trimmed Mean of M-values) method. A design matrix was constructed based on the experimental conditions. Dispersion estimates were obtained using the estimateDisp function, which applies edgeR's empirical Bayes approach. A quasi-likelihood negative binomial model was then fitted using glmQLFit, and differential expression testing was performed with glmQLFTest. Genes were considered differentially expressed if they had an absolute $\log_2$ fold change greater than 1 and a false discovery rate (FDR) below 0.05, corrected using the Benjamini–Hochberg method.

Data availability statement

The raw and processed data generated in this study have been deposited in the NCBI Gene Expression Omnibus (GEO) repository and are publicly available. GeoMx DSP spatial transcriptomic data are accessible under accession number GSE336517, and bulk RNA-seq data are accessible under accession number GSE336518.

Results

Human PDAC contains multinucleated macrophages exhibiting features of giant cells. To evaluate the occurrence of $CD68^+$ MGCs in human pancreatic cancer, we used a set of 145 PDAC specimens stained with an anti-CD68 (12) (**Figure 1A**). MGCs were visually detected in 28% of cases (n=41 specimens out of 145) (**Figure 1B, left**), with a frequency ranging from less than 10 MGCs/slide to more than 50 MGCs/slide (**Figure 1B, right**). The morphological features of MGCs, including number of nuclei and cell shape, exhibited substantial variability across specimens, ranging from round cells containing few nuclei to elongated cells with numerous nuclei (**Figure 1C**). In PDAC sections co-stained with a CD68 and a Pan-cytokeratin antibody no colocalization was detected, confirming that MGCs were *bona fide* $CD68^+$ macrophages and not Pan-cytokeratin$^+$ tumor cells expressing the marker CD68 or macrophages that had fused with tumor cells (26) (**Figure 1D, Supplementary Figure S1A**). This also indicated that MGCs were in contact but excluded from tumor islands (**Figure 1E, Supplementary Figure S1B**). To further confirm the myeloid lineage of MGCs, we performed immunohistochemical staining for PU.1 (SPI1), a nuclear transcription factor expressed in macrophages and other myeloid cells but not in non-hematopoietic epithelial tissues (27). MGCs showed clear nuclear PU.1 positivity (**Figure 1F**), providing independent validation of their macrophage origin. The presence of MGCs did not correlate with the abundance of $CD68^+$ macrophages (**Supplementary Figure S1C**). Because multinucleated macrophages are a hallmark component of granulomas (1), frequent in conditions such as tuberculosis, but also documented in head and neck cancers (6), we investigated whether their occurrence in PDAC tissues was associated with granulomatous structures. In contrast to lung sections from patients with tuberculosis, where Langhans cells were located at the periphery of granulomas (**Figure 1G, left**), MGCs in PDAC sections were never observed in association with granulomatous reactions (**Figure 1G, right**), suggesting that they may arise through distinct mechanisms. Instead, in some cases, MGCs were found in proximity to cholesterol clefts (**Figure 1G, right**).

MGCs in human PDAC have a distinct transcriptional profile compared to MGCs in other pathologies. To characterize tumor-associated MGCs, we compared their morphology in human PDAC with Langhans cells in lung tissues from patients with tuberculosis and MGCs in skin lesions undergoing secondary intention healing (**Figure 2A**). Langhans cells were localized within granulomas (**Figure 1G**) and exhibited the characteristic circular nuclear

arrangement (**Figure 2B, top**), while skin MGCs displayed scattered nuclei resembling foreign-body giant cells (**Figure 2B, bottom left**). MGCs in PDAC sections exhibited a nuclear distribution pattern similar to that observed in skin lesion MGCs, with a more irregular arrangement of nuclei (**Figure 2B, bottom right**). The maximal size of MGCs in PDAC reached 8,358 μm^2, which was significantly smaller than the size of Langhans cells (p=0.0185 by Mann-Whitney) (**Figure 2C**, **left**). Nuclei per cell ranged from 2 to 60 in MGCs in PDAC, significantly fewer than in Langhans cells (p=0.006 by Mann-Whitney) (**Figure 2C**, **right**). Assessment of canonical macrophage polarization markers HLA-DR and CD163 (**Figure 2D-E**) showed that MGCs in tuberculosis displayed high HLA-DR and minimal CD163 expression, consistent with an M1-like profile, while skin lesion MGCs showed heterogeneous expression of both markers. In contrast, MGCs in PDAC lacked both HLA-DR and CD163 (**Figure 2D-E**), indicating that they do not align with conventional polarization states. To capture the profile of MGCs, we performed a spatial transcriptomic analysis using the GeoMx platform, comparing, for each pathology, ROIs containing $CD68^+$ MGCs to ROIs containing $CD68^+$ mononucleated macrophages (Mϕ) (**Figure 2F**). Differential gene expression analysis identified 879 genes distinguishing MGCs from Mϕ in PDAC (**Figure 2G**), confirming that PDAC-associated MGCs are a distinct macrophage population. Fewer genes were modulated in Langhans cells (444; **Supplementary Figure S1D**) and in skin MGCs (104; **Supplementary Figure S1E**) compared to their mononuclear counterparts. In PDAC-associated MGCs, the three most upregulated genes were *MMP9*, *CTSK*, and *ACP5*, all canonical markers of human osteoclasts (28) (**Figure 2G**). In addition, PDAC-associated MGCs exhibited significant upregulation of multiple genes downstream of MYC (*NDRG1*, *COX5A*, *VDAC1*) and gene ontology enrichment analysis revealed that the MYC signaling pathway was the most significantly enriched compared to Mϕ (**Figure 2H, Supplementary Figure S1F**). Additional enriched pathways included mTORC signaling (*MAP2K*3, *CYB5B*, *BHLHE40*), unfolded protein response (*ATF4*, *CALR*, *HSPA9*), bone remodeling (*SPP1*, *TCIRG1*, *MMP9*, *CTSK*, *ACP5*), reactive oxygen species (ROS) production (*ATP6*-, *NDUFA4*), DNA repair (*POLR2K*, *ADRM1*, *GUK1*), epithelial-to-mesenchymal transition (EMT) (*SPP1*, *COL6A2*, *VIM, TGFB1*), hypoxia (*HMOX1*, *ALDOA*, *ENO1*, *ANXA2P1*), TGF-β signaling (*TGFB1*, *RAB31*), mitotic spindle regulation (*YWHAG*, *SEM1*, *PSMD14*), and p53 (*CDKN1A*, *SPHK1*, *HINT1*) (**Figure 2H**, **Supplementary Figure S1F**). Moreover, PDAC-associated MGCs expressed *SPP1*, a gene consistently associated to pro-tumor TAMs in different cancer types (29, 30), but not *TREM2*, differently from MGCs associated with head and neck cancers (6). Some of these

pathways (e.g. hypoxia and extracellular matrix remodelling) were also enriched in Langhans cells in tuberculosis (**Supplementary Figure S1G**), while scar-associated MGCs shared with PDAC-MGC the enrichment in the ROS production, hypoxia and bone remodelling pathways (**Supplementary Figure S1H**). Intersections of both upregulated and downregulated genes confirmed that PDAC-MGCs exhibited the most distinct transcriptional profile overall, accounting for up to 62% of upregulated genes and 56% of downregulated genes (**Supplementary Figure S1I**). Among the genes uniquely expressed by PDAC-associated MGCs were *POLR2K* (involved in DNA repair), *TUBA8* (involved in DNA damage response [DDR]), *COX5B* (involved in control of ROS production), *VDAC1* (a MYC target) and *ANKH* (involved in control of ossification) (**Figure 2I**), confirming the unique profile of cells undergoing DNA damage. To further validate MYC pathway activation at the genomic level, we performed FISH for *MYC* on PDAC sections. MGCs displayed a significantly increased *MYC* copy number compared to Mϕ (**Figure 2J–K, Supplementary Figure S1J**).

MGCs in human PDAC are driven by hypoxia and associated with the squamous molecular subtype. We next investigated which tumor-derived signals might promote the formation of MGCs in human PDAC. To this end, we compared the transcriptomic profiles of tumor cells located in close proximity to MGCs with those situated farther away (**Figure 3A, Supplementary Figure S2A**). Tumor cells adjacent to MGCs showed upregulation of genes and pathways related to hypoxia (*S100A4*, *SERPINE1*, *SLC2A3*), extracellular matrix remodeling (*CTSK*, *TIMP1*, *MMP9*), IFN-α signaling (*IFI30*, *ISG15*, *CD74*), and p53 activation (**Figure 3B–C**). These findings suggested that a hypoxic and matrix-remodeling tumor microenvironment may drive macrophage multinucleation and the emergence of MGCs in pancreatic cancer. To validate this, we set up an *in vitro* model to expose macrophages to hypoxia (**Figure 3D**). The number of MGCs significantly increased following 48h of hypoxic exposure compared with normoxic controls (**Figure 3E**). Activation of the MYC pathway (**Figure 2G-H**) and metabolic adaptations to hypoxia are typically associated with the squamous molecular subtype of pancreatic cancer, according to Bailey *et al*. (31). In line with this, the abundance of MGCs was significantly higher in regions annotated as non-glandular/squamous (p=0.01 by chi-square) (21) (**Figure 3F-G**). To explore the association of MGCs with the squamous molecular subtype in publicly available datasets, we identified a MGC gene signature, after filtering genes expressed by tumor cells (**Supplementary Figure S2B**), and probed it in TCGA. Specifically, the signature included *CD68*, a macrophage lineage

marker; *HMOX1*, which is involved in response to oxidative stress; *CD276*, which is an immune checkpoint involved in macrophage efferocytosis (32); and *ICAM1*, *MMP9* and *ANPEP,* all of which are associated with macrophages remodeling functions. Moreover, it included *ITGAV* and *NDRG1,* two MYC targets. In a cohort of 170 PDAC cases from TCGA, dataset PAAD, the MGC signature was found to be significantly enriched in samples classified as "squamous" compared to the ones classified as "classical" (p=0.0026 by Mann Whitney) (**Figure 3H**). To evaluate its prognostic relevance, GSVA scores were computed for each sample and patients were stratified using a predefined thresholding approach based on the median absolute deviation ± 5% (MAD), excluding intermediate cases. Using this strategy, patients with a high MGC score (MGChi, n=82) displayed significantly shorter overall survival compared with patients with a low MGC score (MGClo, n=83) (p=0.049 by log-rank Mantel–Cox test) (**Figure 3I**).

MGCs are a correlate of neoadjuvant chemotherapy in human PDAC. In the institutional PDAC cohort, the frequency of patients with MGCs compared to patients without MGCs was different among patients who did not receive neoadjuvant chemotherapy (NAT NO) and patients who received it (NAT YES) (35% vs 46% respectively) (**Figure 4A**), suggesting that MGCs are a correlate of chemotherapy. This effect was particularly observed among patients treated with gemcitabine (**Figure 4B**). To directly assess whether chemotherapy could promote macrophage multinucleation, *in vitro*–differentiated macrophages were treated with gemcitabine (GEM) or paclitaxel (PTX). Both treatments increased the percentage of MGCs compared to control conditions (**Figure 4C**). Bulk RNA sequencing analysis of PDAC tissues from NAT treated or untreated patients (**Figure 4D**) highlighted enrichment of genes and pathways similar to the ones found in MGCs (**Figure 2H**), including myogenesis (*DES* and *SOD3* being the most up-regulated genes), hypoxia (*FOS*, *DUSP1*), MYC targets, ROS, and p53 (**Figure 4E-F**), among those treated with NAT, suggesting that chemotherapy might induce the occurrence of multinucleation in macrophages, as a response to tissue damage. In line with the fact that fibrosis is a hallmark of tissue response to chemotherapy in human PDAC (33, 34), the percentage of fibrosis, as assessed by picrosirius red staining, was higher in specimens from NAT treated versus untreated patients (**Figure 4G-I**).

MGCs in human PDAC have an altered nuclear morphology and exhibit signs of an activated DDR. Even though the transcriptomic profile of PDAC-associated MGCs was enriched in genes and pathways related to bone remodeling, MGCs did not specifically

upregulate genes related to fusion, suggesting that the mechanisms of macrophage polyploidization in PDAC could be different to those in bone. In contrast, PDAC-associated MGCs were associated with NAT, which can induce tissue damage. To further investigate this, we focused on nuclear metrics of MGCs. Deviations in nuclear morphology or organization affect cellular functions and are known to trigger specific gene-expression pathways. At the same time, inflammatory stimuli induce morphological and mechanical remodeling of macrophage nuclei (35). Nuclei in PDAC-associated MGCs appeared more irregular in morphology and distribution compared to those in Langhans cells in tuberculosis or in MGC in skin lesions at visual inspection (**Figure 5A**), a finding also confirmed by super resolution images of staining with an antibody specific for Lamin B1, a nuclear membrane protein (**Figure 5B, Supplementary Figure S3A**). We quantified nuclear metrics traditionally applied to epithelial cancer cells, such as the distance between the nuclei and the membrane, the circularity index (which measures the uniformity of nuclear distribution around the cell centroid), and the spread index (which reflects the dispersion of nuclei around the centroid) (**Supplementary Figure S3B**). In PDAC-associated MGCs the distance of nuclei to the cell membrane was significantly higher than in tuberculosis and skin MGCs ($p<0.0001$ compared to tuberculosis and $p=0.0018$ compared to skin lesions) (**Supplementary Figure S3C, left**). This was accompanied by lower circularity index ($p<0.0001$ and $p<0.005$ respectively by Mann Whitney) (**Supplementary Figure S3C, middle**) and an increased nuclear spread index ($p=0.0003$ compared to tuberculosis and $p=0.0078$ compared to skin lesions) (**Supplementary Figure S3C, right**), consistent with the more random distribution of the nuclei observed in PDAC-associated MGCs (**Figure 5A**). In PDAC-associated MGCs, nuclear area, a strong correlate of DNA content, was significantly higher than in Mϕ (**Figure 5C**), suggesting alterations in nuclear DNA content, which would be consistent with the enrichment in the DNA repair and p53 pathways (**Figure 2H**). To get insights into the cues driving multinucleation in PDAC-associated MGCs, we assessed the DDR, by staining PDAC tissue sections with an antibody against p53-binding protein 1 (53BP1), a molecule rapidly localizing at DNA damage sites to activate the downstream repair process. The number of $53BP1^+$ nuclei was significantly higher in MGCs compared to Mϕ (**Figure 5D-E**). Additionally, a significantly greater number of MGC nuclei stained positive for the proliferation marker Ki67 relative to Mϕ (**Figure 5F-G**). MGCs also exhibited a higher frequency of nuclei co-expressing 53BP1 and Ki67 (**Figure 5F-G** and **Supplementary Figure S3D**). Overall, the ongoing proliferation and the increased number of nuclei accumulating 53BP1 point to the activation of a DDR in PDAC-associated

MGCs. To further investigate the mechanisms underlying macrophage multinucleation, we assessed the contribution of MYC signaling, which was enriched in PDAC-associated MGCs (**Figure 2H**) and in chemotherapy-treated tissues (**Figure 4F**). Pharmacological inhibition of MYC with 10058-F4 markedly reduced the formation of MGCs *in vitro*, even under hypoxic conditions, indicating that MYC activity was required for hypoxia-driven multinucleation (**Figure 5H-I**). To determine whether hypoxia-induced MGCs recapitulate the phenotype observed in human PDAC tissues, we performed IF analyses on *in vitro* cultures. These cells retained expression of the myeloid lineage marker PU.1, lacked CD163 expression, consistent with the non-canonical polarization state observe in PDAC-MGCs (**Figure 2D**), and displayed 53BP1^{+} nuclear foci (**Figure 5J)**, indicative of activation of a DDR. Collectively, these findings support the hypothesis that hypoxia-driven multinucleation reproduces key phenotypic features of PDAC-associated MGCs.

Discussion

The diversity of TAMs in human cancer has been the object of intense studies (16, 36), which aimed at dissecting their biology and leading to the identification of specific markers and morphological features of pro- and antitumor TAMs (30). Since morphological features of macrophages correlate with their function (15, 16), we focused on TAM morphology and identified polyploid macrophages exhibiting characteristics of MGCs. Compared to multinucleated macrophages found in other non-neoplastic inflammatory conditions, i.e. Langhans cells or multinucleated macrophages in foreign-body responses, PDAC-associated MGCs lacked expression of M1-like or M2-like markers and displayed a distinct transcriptomic profile, particularly enriched in pathways related to MYC activation, hypoxia, ROS generation, and DDR. These features suggest that, rather than representing a polarized macrophage subset, PDAC-associated MGCs reflect a stress-adaptive macrophage state shaped by chronic exposure to hypoxia and genotoxic signals within the tumor microenvironment. Differently from MGCs described recently in head and neck cancers (6), PDAC-associated MGCs did not upregulate *TREM2*, a hallmark gene in MGCs in head and neck cancer. This could be explained by the fact that in PDAC, TAMs express TREM2 (37), and suggests that MGCs in different tumors may form by distinct mechanisms. Conventional scRNA-seq datasets are unlikely to efficiently capture large MGCs, which may be lost during tissue dissociation or excluded during standard doublet filtering. Although our transcriptomic profiling was not performed at single-cell resolution, the molecular features identified in MGC-rich regions were supported by independent *in vitro* experiments, which recapitulated key pathways observed *in vivo*, including MYC activation and hypoxia-related programs.

Most studies investigating the mechanisms of formation of MGCs have drawn insights from osteoclasts, their well-characterized homeostatic counterpart. Osteoclastogenesis is driven by cell fusion in response to RANKL signaling (18). Similarly, the formation of MGCs has been attributed to a cell fusion process involving several coordinated steps and key molecules, including chemoattractants, metalloproteinases, and membrane proteins (2). Even though the transcriptomic profile of PDAC-associated MGCs was enriched in genes and pathways related to bone remodeling, MGCs did not specifically upregulated genes related to fusion, suggesting that the mechanisms of macrophage polyploidization in PDAC could be different.

Recent evidence has shown that macrophages accumulate multiple nuclei after unscheduled genome duplication, often triggered in response to persistent stimuli, including mycobacteria or the foreign body response (1, 38), in the context of a DDR (39). Polyploidization associated with DDR has been documented for tumor cells, where chronic DNA damage can lead to mitotic bypass and tetraploidy (40). Similarly, in non-alcoholic fatty liver disease, oxidative stress drives pathological polyploidization of hepatocytes (41). Notably, the DDR has a role also in immune cells and encompasses regulation of innate immunity, macrophage reprogramming, lymphocyte development (42). Our results point to the activation of a DDR in PDAC MGCs, which have increased number of nuclei accumulating 53BP1, a molecule rapidly localizing at DNA damage sites to activate the downstream repair process.

Three interconnected pathways could contribute to DDR and MGC generation in PDAC according to the gene ontology analysis, namely ROS production, hypoxia, and MYC activation. Hypoxia is a well-known factor affecting genomic instability and triggering the DDR (43). Hypoxia-related transcriptional programs can occur in multiple cellular compartments within the tumor microenvironment; in our spatial analysis, tumor-derived transcriptional changes evaluated in PanCK$^+$ AOIs indicated a hypoxia signature associated with MGC proximity, reflecting tumor cell responses to hypoxic stress. Release of reactive oxygen and nitrogen species by phagocytes serves as a critical antibacterial defense mechanism through the induction of genotoxic stress (38), but macrophages themselves are susceptible to the effect of genotoxic agents that can ultimately damage their DNA and activate the DDR pathway (39), as well as the STING pathway and type I IFN response (44, 45). Furthermore, altered ROS regulation is known to be associated with macrophage multinucleation in chronic granulomatous disease (CGD) (43). Finally, the DDR is also consistent with the enrichment in MYC pathways, since this transcription factor regulates cellular proliferation and growth, and it is known to induce replication stress, which is intrinsically linked to the DDR (39). Consistently, FISH analysis revealed increased MYC copy number in multinucleated macrophages compared to mononucleated counterparts, supporting enhanced MYC activity in this cell population. In a model of macrophage polyploidization achieved after persistent inflammatory stimulation with bacterial products, MYC–DDR signaling was found to be relevant for genomic stability during the formation of polyploid macrophages (39). MYC is induced in macrophages polarized in vitro by IL-4 and transcriptionally regulates the expression of M2-associated genes (46, 47) and negatively regulates inflammatory activation

of macrophages (48). Moreover, N-MYC downstream regulated gene 1 (NDRG1) a DNA repair protein recently found to mediate resistance to chemotherapy in human PDAC (49), was upregulated in MGCs.

The occurrence of MGCs in human tumor tissues raises questions as to whether these cells participate in immune surveillance, contribute to immunosuppressive niches, or represent a tissue repair mechanism. To identify tumor-derived signals potentially involved in polyploidization, we looked at tumor cells in closed proximity with MGCs and their profile indicated hypoxia, inflammation, p53, UV response. In head and neck cancers, granulomas surrounding keratin debris composed of TREM2-expressing MGCs have been evaluated as biomarkers associated to favorable prognosis (6). We did not have evidence of granulomas in PDAC tissues and MGCs were always found scattered in the tissue, rather than concentrated in specific architectural areas (such as granulomas). Therefore, the contradictory results on the clinical relevance of MGCs in different tumor contexts may be due to their association with granulomas, which is frequent but not universal, and to the fact that they form by distinct mechanisms.

Although MGCs were detected in 28% of PDAC specimens in our cohort, this population has not been systematically reported in previous studies. This may reflect a predominant focus on macrophage density and polarization markers rather than on morphological assessment and, especially in routine diagnostic practice, immune cell morphology not directly relevant for tumor classification may have remained under-recognized. MGCs have been described in rare giant cell–containing pancreatic lesions, such as undifferentiated carcinoma with osteoclast-like giant cells (20) or giant cell tumors of soft tissue (19). It is therefore possible that their presence in other pancreatic pathological contexts has been under-recognized. In our cohort, however, these entities were systematically excluded by expert pathological review. A foreign-body type giant cell reaction is contemplated as a criterium of assessment of the pathological response to NAT (33), confirming our findings of an association of multinucleation of macrophages with perioperative treatment. In light of our results, a possible explanation might be that prolonged immune activation and tissue stress are drivers of multinucleation in macrophages after tissue exposure to NAT. On these premises, the identification of MGC-based classifiers may contribute to implement current criteria of response to NAT, capturing the heterogeneous response to treatment. In particular, identification of morphological and

nuclear metrics distinctive of MGCs may lay the groundwork for further classification efforts based on image-derived features.

Acknowledgments

Federica Marchesi and Vincenzo Corbo are founders of the Italian Pancreatic Cancer Community (iPCC). We thank all the members of iPCC for fruitful discussion, and in particular Dr. Elisa Giovannetti for valuable advice on experiments involving chemotherapeutic agents. We thank Fondazione Nadia Valsecchi for continuous support to our research. The authors used generative artificial intelligence tools solely to assist with language editing and clarity of the manuscript. All scientific content, data interpretation, and conclusions were developed entirely by the authors.

References

1. Ramakrishnan L. Revisiting the role of the granuloma in tuberculosis. Nat Rev Immunol. 2012;12(5):352–66.
2. Brooks PJ, Glogauer M, McCulloch CA. An Overview of the Derivation and Function of Multinucleated Giant Cells and Their Role in Pathologic Processes. Am J Pathol. 2019;189(6):1145–58.
3. Ahmadzadeh K, Vanoppen M, Rose CD, Matthys P, Wouters CH. Multinucleated Giant Cells: Current Insights in Phenotype, Biological Activities, and Mechanism of Formation. Front Cell Dev Biol. 2022;10:873226.
4. Sangaletti S, Ferrara R, Tripodo C, Garassino MC, Colombo MP. Myeloid cell heterogeneity in lung cancer: implication for immunotherapy. Cancer Immunol Immunother. 2021;70(9):2429–38.
5. Wang H, Zhou J, Li J, Geng Y, Meng P, Ma C, et al. A study of multinucleated giant cells in esophageal cancer. Clin Immunol. 2021;222:108600.
6. Gessain G, Anzali AA, Lerousseau M, Mulder K, Bied M, Auperin A, et al. TREM2-Expressing Multinucleated Giant Macrophages Are a Biomarker of Good Prognosis in Head and Neck Squamous Cell Carcinoma. Cancer Discov. 2024;14(12):2352–66.
7. Ahmadzadeh K, Pereira M, Vanoppen M, Bernaerts E, Ko JH, Mitera T, et al. Multinucleation resets human macrophages for specialized functions at the expense of their identity. EMBO Rep. 2023;24(4):e57070.
8. Pagan AJ, Ramakrishnan L. The Formation and Function of Granulomas. Annu Rev Immunol. 2018;36:639–65.
9. Halbrook CJ, Lyssiotis CA, Pasca di Magliano M, Maitra A. Pancreatic cancer: Advances and challenges. Cell. 2023;186(8):1729–54.
10. Shakiba M, Tuveson DA. Macrophages and fibroblasts as regulators of the immune response in pancreatic cancer. Nat Immunol. 2025;26(5):678–91.
11. Vonderheide RH, Bear AS. Tumor-Derived Myeloid Cell Chemoattractants and T Cell Exclusion in Pancreatic Cancer. Front Immunol. 2020;11:605619.
12. Di Caro G, Cortese N, Castino GF, Grizzi F, Gavazzi F, Ridolfi C, et al. Dual prognostic significance of tumour-associated macrophages in human pancreatic adenocarcinoma treated or untreated with chemotherapy. Gut. 2016;65(10):1710–20.
13. Vayrynen SA, Zhang J, Yuan C, Vayrynen JP, Dias Costa A, Williams H, et al. Composition, Spatial Characteristics, and Prognostic Significance of Myeloid Cell Infiltration in Pancreatic Cancer. Clin Cancer Res. 2021;27(4):1069–81.
14. Caronni N, La Terza F, Vittoria FM, Barbiera G, Mezzanzanica L, Cuzzola V, et al. IL-1beta(+) macrophages fuel pathogenic inflammation in pancreatic cancer. Nature. 2023;623(7986):415–22.
15. Donadon M, Torzilli G, Cortese N, Soldani C, Di Tommaso L, Franceschini B, et al. Macrophage morphology correlates with single-cell diversity and prognosis in colorectal liver metastasis. J Exp Med. 2020;217(11):e20191847.
16. Mantovani A, Marchesi F, Di Mitri D, Garlanda C. Macrophage diversity in cancer dissemination and metastasis. Cell Mol Immunol. 2024;21(11):1201–14.
17. Milde R, Ritter J, Tennent GA, Loesch A, Martinez FO, Gordon S, et al. Multinucleated Giant Cells Are Specialized for Complement-Mediated Phagocytosis and Large Target Destruction. Cell Rep. 2015;13(9):1937–48.
18. Helming L, Gordon S. Molecular mediators of macrophage fusion. Trends Cell Biol. 2009;19(10):514–22.
19. Dehner C DL. PathologyOutlinescom. 2021.
20. Luchini C. Undifferentiated carcinoma with osteoclast-like giant cells. PathologyOutlinescom. 2022.

21. Di Chiaro P, Nacci L, Arco F, Brandini S, Polletti S, Palamidessi A, et al. Mapping functional to morphological variation reveals the basis of regional extracellular matrix subversion and nerve invasion in pancreatic cancer. Cancer Cell. 2024;42(4):662–81 e10.
22. Rigamonti A, Viatore M, Polidori R, Rahal D, Erreni M, Fumagalli MR, et al. Integrating AI-Powered Digital Pathology and Imaging Mass Cytometry Identifies Key Classifiers of Tumor Cells, Stroma, and Immune Cells in Non-Small Cell Lung Cancer. Cancer Res. 2024;84(7):1165–77.
23. Erreni M, Fumagalli MR, Zanini D, Candiello E, Tiberi G, Parente R, et al. Multiplexed Imaging Mass Cytometry Analysis in Preclinical Models of Pancreatic Cancer. Int J Mol Sci. 2024;25(3).
24. Veghini L, Pasini D, Fang R, Delfino P, Filippini D, Neander C, et al. Differential activity of MAPK signalling defines fibroblast subtypes in pancreatic cancer. Nat Commun. 2024;15(1):10534.
25. Moffitt RA, Marayati R, Flate EL, Volmar KE, Loeza SG, Hoadley KA, et al. Virtual microdissection identifies distinct tumor- and stroma-specific subtypes of pancreatic ductal adenocarcinoma. Nat Genet. 2015;47(10):1168–78.
26. Powell AE, Anderson EC, Davies PS, Silk AD, Pelz C, Impey S, et al. Fusion between Intestinal epithelial cells and macrophages in a cancer context results in nuclear reprogramming. Cancer Res. 2011;71(4):1497–505.
27. Rosenbauer F, Tenen DG. Transcription factors in myeloid development: balancing differentiation with transformation. Nat Rev Immunol. 2007;7(2):105–17.
28. Hansen MS, Madsen K, Price M, Soe K, Omata Y, Zaiss MM, et al. Transcriptional reprogramming during human osteoclast differentiation identifies regulators of osteoclast activity. Bone Res. 2024;12(1):5.
29. Zhang L, Li Z, Skrzypczynska KM, Fang Q, Zhang W, O'Brien SA, et al. Single-Cell Analyses Inform Mechanisms of Myeloid-Targeted Therapies in Colon Cancer. Cell. 2020;181(2):442–59 e29.
30. Cortese N, Carriero R, Barbagallo M, Putignano AR, Costa G, Giavazzi F, et al. High-Resolution Analysis of Mononuclear Phagocytes Reveals GPNMB as a Prognostic Marker in Human Colorectal Liver Metastasis. Cancer Immunol Res. 2023;11(4):405–20.
31. Bailey P, Chang DK, Nones K, Johns AL, Patch AM, Gingras MC, et al. Genomic analyses identify molecular subtypes of pancreatic cancer. Nature. 2016;531(7592):47–52.
32. Cheng M, Chen S, Li K, Wang G, Xiong G, Ling R, et al. CD276-dependent efferocytosis by tumor-associated macrophages promotes immune evasion in bladder cancer. Nat Commun. 2024;15(1):2818.
33. Kalimuthu S, Serra S, Dhani N, Hafezi-Bakhtiari S, Szentgyorgyi E, Vajpeyi R, et al. Regression grading in neoadjuvant treated pancreatic cancer: an interobserver study. J Clin Pathol. 2017;70(3):237–43.
34. Springfeld C, Ferrone CR, Katz MHG, Philip PA, Hong TS, Hackert T, et al. Neoadjuvant therapy for pancreatic cancer. Nat Rev Clin Oncol. 2023;20(5):318–37.
35. Jiao S, Li C, Guo F, Zhang J, Zhang H, Cao Z, et al. SUN1/2 controls macrophage polarization via modulating nuclear size and stiffness. Nat Commun. 2023;14(1):6416.
36. Locati M, Curtale G, Mantovani A. Diversity, Mechanisms, and Significance of Macrophage Plasticity. Annu Rev Pathol. 2020;15:123–47.
37. Papakonstantinou D, Wang H, Bani MA, Mulder K, Dunsmore G, Boileve A, et al. Molecular analysis highlights TREM2 as a discriminating biomarker for patients suffering from pancreatic ductal adenocarcinoma. Cancer Treat Res Commun. 2025;43:100939.
38. Horn V, Triantafyllopoulou A. DNA damage signaling and polyploid macrophages in chronic inflammation. Curr Opin Immunol. 2018;50:55–63.

39. Herrtwich L, Nanda I, Evangelou K, Nikolova T, Horn V, Sagar, et al. DNA Damage Signaling Instructs Polyploid Macrophage Fate in Granulomas. Cell. 2018;174(5):1325–6.
40. Davoli T, Denchi EL, de Lange T. Persistent telomere damage induces bypass of mitosis and tetraploidy. Cell. 2010;141(1):81–93.
41. Gentric G, Maillet V, Paradis V, Couton D, L'Hermitte A, Panasyuk G, et al. Oxidative stress promotes pathologic polyploidization in nonalcoholic fatty liver disease. J Clin Invest. 2015;125(3):981–92.
42. Kasapi A, Triantafyllopoulou A. Genotoxic stress signalling as a driver of macrophage diversity. Cell Stress. 2022;6(3):30–44.
43. Suvac A, Ashton J, Bristow RG. Tumour hypoxia in driving genomic instability and tumour evolution. Nat Rev Cancer. 2025;25(3):167–88.
44. Hartlova A, Erttmann SF, Raffi FA, Schmalz AM, Resch U, Anugula S, et al. DNA damage primes the type I interferon system via the cytosolic DNA sensor STING to promote anti-microbial innate immunity. Immunity. 2015;42(2):332–43.
45. Morales AJ, Carrero JA, Hung PJ, Tubbs AT, Andrews JM, Edelson BT, et al. A type I IFN-dependent DNA damage response regulates the genetic program and inflammasome activation in macrophages. Elife. 2017;6.
46. Martinez FO, Helming L, Milde R, Varin A, Melgert BN, Draijer C, et al. Genetic programs expressed in resting and IL-4 alternatively activated mouse and human macrophages: similarities and differences. Blood. 2013;121(9):e57–69.
47. Pello OM, De Pizzol M, Mirolo M, Soucek L, Zammataro L, Amabile A, et al. Role of c-MYC in alternative activation of human macrophages and tumor-associated macrophage biology. Blood. 2012;119(2):411–21.
48. Bae S, Park PSU, Lee Y, Mun SH, Giannopoulou E, Fujii T, et al. MYC-mediated early glycolysis negatively regulates proinflammatory responses by controlling IRF4 in inflammatory macrophages. Cell Rep. 2021;35(11):109264.
49. Kozlova N, Cruz KA, Doh HM, Ruzette AA, Willis NA, Hong SM, et al. A novel DNA repair protein, N-Myc downstream regulated gene 1 (NDRG1), links stromal tumour microenvironment to chemoresistance. bioRxiv. 2025.

Figure Legends

Figure 1. Occurrence of multinucleated giant cells in human pancreatic adenocarcinoma. (**A**) Representative whole slide immunohistochemistry of $CD68^+$ cells (brown) in a PDAC specimen. Scale bar 200 µm. The inset shows some multinucleated macrophages. Scale bar 50 µm. (**B**) Frequency of MGCs in PDAC tissues among n=145 analyzed samples. In **left** panel, dots represent the number of MGCs in each specimen, grouped according to absence (w/o MGC) or presence (w MGC) of MGCs. In **right** panel, distribution of MGCs in 145 tissues is shown, stratifying samples according to the number of MGCs per specimen: no detectable MGCs, fewer than 10 MGCs, between 10 and 49 MGCs, and 50 or more MGCs. Box and whiskers represent Min to Max and median of the distribution. (**C**) Representative pictures of MGCs showing marked variability in morphological features and number of nuclei. Scale bar 20 µm. (**D**) Double staining with an anti-CD68 (green) and anti-Pan-cytokeratin (red) on a PDAC section. (**E**) Representative images of $CD68^+$ MGCs (green) and $PanCK^+$ tumor cells (red) in human PDAC sections, allowing to appreciate the localization of MGCs excluded from tumor glands. Dotted lines delineate tumor regions. Scale bar 200 µm. (**F**) Immunohistochemical staining for CD68 (left) and PU.1 (brown nuclear signal, **right**) in PDAC sections. MGCs (outlined by dotted circles) display nuclear PU.1 positivity, confirming the myeloid lineage. Scale bar 100 µm. (**G**) Representative whole slide images of tuberculosis (**left**) and PDAC (**right**) tissues. In tuberculosis, MGCs (red) localize within granulomas, whereas in PDAC MGCs are not associated with granulomatous structures and occasionally observed adjacent to cholesterol clefts. Scale bar 2mm.

Figure 2. **Transcriptomic profile of MGCs in human pancreatic cancer.** (**A**) Schematic representation of the comparative study used to analyze MGCs in different pathological contexts, i.e. lung tissues from patients with tuberculosis, skin lesions undergoing secondary intention healing and human pancreatic cancer (performed with *Biorender.com*). (**B**) Three exemplifying pictures of multinucleated macrophages in human tuberculosis (**up**), skin (**bottom left**) and PDAC (**bottom right**) tissues. Scale bar 50 µm. (**C**) Morphological metrics of MGCs in human pathological conditions. Box and whiskers represent Min to Max and median of 60 cells analyzed (n=3 specimens each pathological condition; *p=0.0185 and ***p=0.0003 [cell area]; *p=0.02 and **p=0.0065 [n° of nuclei] by Mann-Whitney test). (**D**) Expression of CD163 and HLA-DR markers by imaging mass cytometry on $CD68^+$ MGCs in tuberculosis, skin lesion and PDAC tissues. Distinct MGCs are outlined. (**E**) Differential expression of CD163 and HLA-DR in mononucleated Mϕ and MGCs across tissues (n=7 specimens, 8 ROIs/specimen). Histograms represent the percentage of cells positive to the markers. Box and whiskers represent Min to Max and median of the distribution. **p<0.005 and ****p<0.0001 by Mann-Whitney test. (**F**) Schematic of the spatial transcriptomic analysis of MGCs in human sections from different pathologies. Representative images of 2 ROIs (without and with MGCs) stained with SYTO13 (blue), CD68 (green) and scanned on the Nanostring GeoMx® platform. (**G**) Volcano plot showing differentially expressed genes between ROIs with MGCs versus ROIs without MGCs in human PDAC sections. Exemplar genes are labelled. Up regulated genes (blue) and down regulated genes (orange) by [log2(fold

change) > |0.58| and adjusted P value < 0.01]. Adjusted p values via limma (eBayes) and Benjamini–Hochberg correction. (**H**) Pre-ranked Gene Set Enrichment Analysis in MGCs showing selected Gene Ontology Biological Process and Reactome annotations. NES (Normalized Enrichment Score) by color-code and log10 (adjusted pvalue) by size of the balloon. P value via adaptive multilevel Monte Carlo, adjusted by Benjamini–Hochberg. (**I**) Violin plots showing the log-normalized counts (logCPM) of selected genes from ROIs with MGC and ROIs without MGCs (Mϕ). Adjusted p values via limma (eBayes) and Benjamini–Hochberg correction. **(J)** Representative fluorescence in situ hybridization (FISH) image of a PDAC section showing nuclei stained with DAPI (blue) and MYC signal (red). The inset highlights a MGC (dashed outline) compared with surrounding mononucleated cells. (**K**) Quantification of MYC FISH signal in Mϕ and MGCs. Each dot represents a single cell (n=200 cells from 4 ROIs per patient, two PDAC samples). Statistical significance was assessed using the Mann–Whitney test (****p < 0.0001).

Figure 3. **MGCs in human PDAC are associated with the squamous molecular subtype, and hypoxia.** (**A**) Representative images of 2 ROIs (with tumor cells far (**top**) or closed (**bottom**) to MGCs) stained with PanCK (red), CD68 (green) and SYTO13 (blue). The transcriptome from PanCK$^+$ tumor cells is then processed through the Digital Spatial Profiling platform. (**B**) Gene Set Enrichment Analysis from tumor cells closed to MGCs, showing selected Hallmark annotations. (**C**) Violin plots showing log-normalized expression levels (logCPM) of selected genes belonging to pathways enriched in ROIs closed to MGCs. Adjusted p values via limma (eBayes) and Benjamini–Hochberg correction. (**D**) Representative pictures of cells cultured under normoxic (Control) or hypoxic (48 h) conditions showing the formation of multinucleated giant cells (MGCs). (**E**) Quantification of the percentage of MGCs under each condition. Box and whiskers represent Min to Max and median of 14 high power fields (HPF) for each condition (****p < 0.0001, unpaired t test with Welch's correction). (**F**) Representative pictures of MGCs in PDAC glandular/classical (**left**) and non-glandular/squamous subtypes (**right**) morphological patterns. Drawings schematize the typical features of the two patterns. Dotted lines outline tumor glands/cells, yellow solid lines outline MGCs. Scale bar 100 μm and 50 μm (insets). (**G**) Pie chart showing percentage of tumor regions annotated as glandular/classical or non-glandular/squamous (n=30; p=0.01 by Chi square). (**H**) Boxplot showing the distribution of the GSVA-derived MGC scores in TCGA-PAAD patients stratified by molecular subtypes (Classical vs Squamous). Box and whiskers represent Min to Max and median of the distribution. P=0.0026 by Wilcoxon rank-sum test. (**I**) Survival curve on TCGA pancreatic cancer (TCGA-PAAD; n=170) dataset based on median expression of gene signature from MGCs. High and low groups are calculated based on the median absolute deviation ± 5% (MAD). P=0.049 by log-rank Mantel–Cox test.

Figure 4. MGCs are a correlate of neoadjuvant chemotherapy in human PDAC. (**A**) Pie charts showing percentage of PDAC tissues with (blue) and without (grey) MGCs in untreated (**left**) and treated (**right**) patients with neoadjuvant chemotherapy. (**B**) Stacked plots showing the proportion of neoadjuvant chemotherapy regimens (Mix (violet), Folfirinox (pink), GnabP (green)) received by PDAC patients, comparing patients with and without MGCs. p=0.056 by

Chi-square test. (**C**) Boxplots of the percentage of MGCs under each condition following treatment with gemcitabine (GEM) or paclitaxel (PTX). Each dot represents an individual well. Data are pooled from three independent experiments, with two wells per condition for each experiment. Box and whiskers represent Min to Max and median of the distribution. Statistical analysis was performed using two-way ANOVA with Dunnett's multiple comparisons test (****$p < 0.0001$). (**D**) Schematic of the work. Transcriptomic analysis of n=16 PDAC sections from patients treated or not with neoadjuvant chemotherapy (NAT) (performed with *Biorender.com*). (**E**) Volcano plot showing differentially expressed genes between NAT treated and untreated PDAC sections. Exemplar genes are labelled. Purple genes represent up regulated genes and blue genes represent down regulated genes [log2(fold change) > |1| and adjusted P value < 0.05]. (**F**) Gene Set Enrichment Analysis in PDAC tissues exposed to NAT, showing selected Hallmark annotations. NES (Normalized Enrichment Score). Only significant pathways are shown; p value via adaptive multilevel Monte Carlo, adjusted by Benjamini–Hochberg. (**G**) Representative images of PDAC sections from untreated and treated samples showing fibrosis (Picrosirius Red), merged images with Picrosirius Red mask (in dark green) and MGC annotations (in brown), and IHC staining showing $CD68^+$ MGCs. (**H**) Quantification of the percentage of fibrotic area in untreated and treated PDAC samples. Box and whiskers represent Min to Max and median (n = 17 for Untreated, n = 20 for Treated; p = 0.0047, unpaired t test with Welch's correction). (**I**) Quantification of the percentage of fibrotic area in PDAC samples with low or high MGC abundance. Box and whiskers represent Min to Max and median (p = 0.0087, unpaired t test with Welch's correction).

Figure 5. MGCs in human pancreatic cancer have an altered nuclear morphology and an active DNA damage response. (**A**) Representative images of MGCs in tuberculosis, skin lesion and PDAC, allowing to appreciate the characteristic nuclear arrangement. Scale bar: 20 µm. (**B**) Representative super-resolution STED image of a PDAC-MGC stained with LaminB1 (red) and CD68 (green). Scale bar: 10 µm. (**C**) Comparison of nuclear area among mononucleated Mϕ and MGCs. Box and whiskers represent Min to Max and median of 18 mononucleated Mϕ and 12 MGCs analyzed (n=3 specimens; ****$p<0.0001$ by Mann-Whitney test). (**D**) Representative immunofluorescence images of human PDAC sections showing $CD68^+$ MGCs (green), $53BP1^+$ nuclei (red), and DAPI (blue). Scale bar 100 µm. (**E**) Quantification of $53BP1^+$ nuclei in $CD68^+$ mononuclear Mϕ versus MGCs in human PDAC. ****$p < 0.0001$ by Mann-Whitney test. (**F**) Representative immunofluorescence images of human PDAC sections showing $CD68^+$ MGCs (green), $53BP1^+$ nuclei (red), $Ki67^+$ nuclei (white), and DAPI (blue). Scale bar 100 µm. (**G**) Quantification of 53BP1 and Ki67 in $CD68^+$ mononucleated Mϕ and MGCs in PDAC tissue sections. For Mϕ, each dot represents the mean percentage of positive nuclei per ROI analyzed (n=7). For MGCs, each dot represents the mean percentage of positive nuclei per individual MGC analyzed (n=7). Analysis performed on n=3 PDAC stained slides. Box and whiskers represent mean with SEM. **$p < 0.01$ and ***$p < 0.001$ by Mann-Whitney test. (**H-I**) Effect of MYC inhibition on hypoxia-induced MGCs formation. (**H**) Representative images of macrophages cultured under normoxia or hypoxia (48 h), with or without the MYC inhibitor 10058-F4. Scale bar 50 µm. (**I**) Quantification of the number of MGCs per condition. Each dot represents one well. Box and whiskers represent Min

to Max and median of the distribution (****$p < 0.0001$ by one-way ANOVA with Tukey's multiple comparisons test). (**J**) Immunofluorescence characterization of hypoxia-induced MGCs. Representative images showing DAPI (white), CD68 (green), PU.1, CD163 and 53BP1 (magenta). Dashed lines outline MGCs. Insets highlight 53BP1 nucleare foci. Scale bar 20 μm.

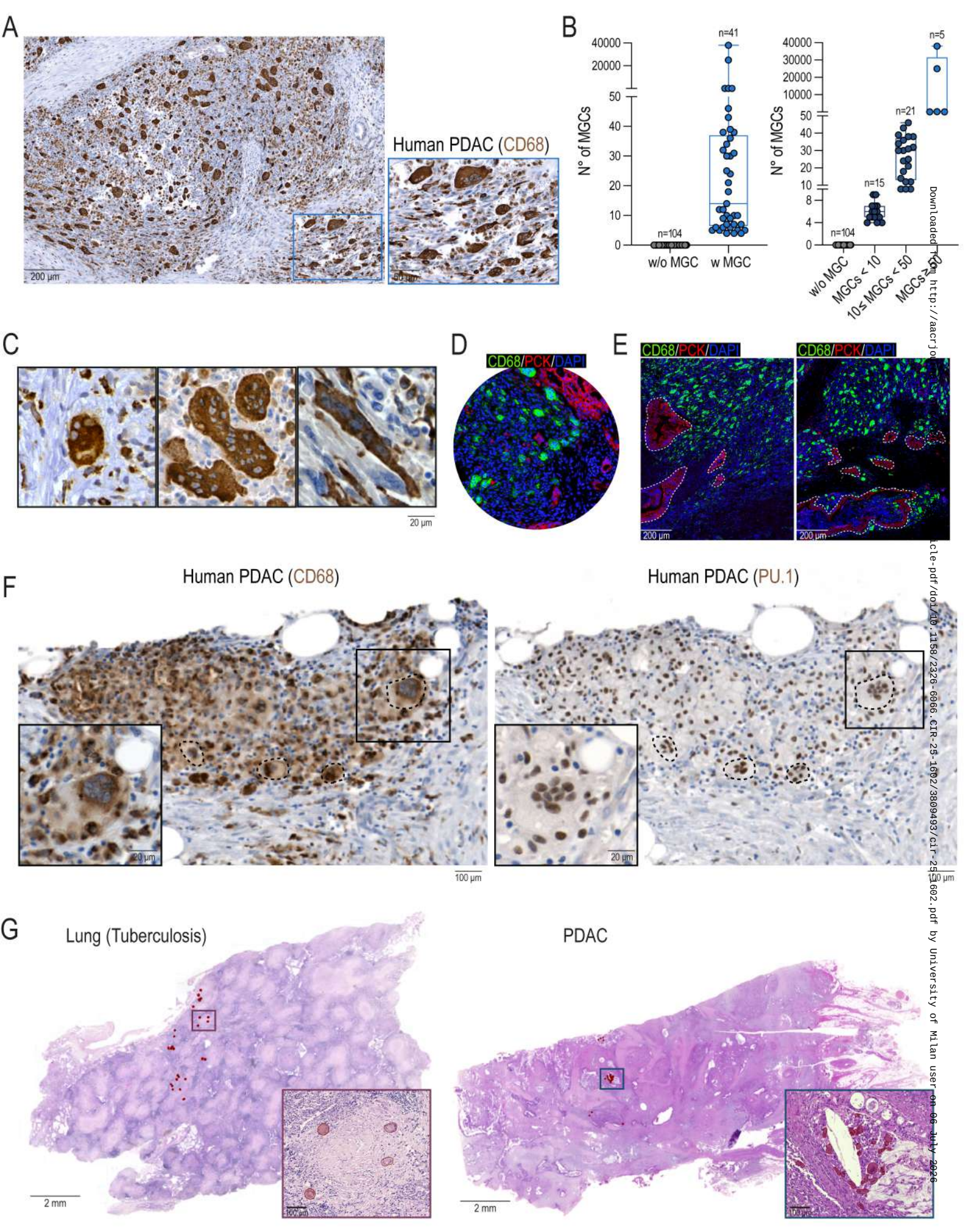

Figure 1

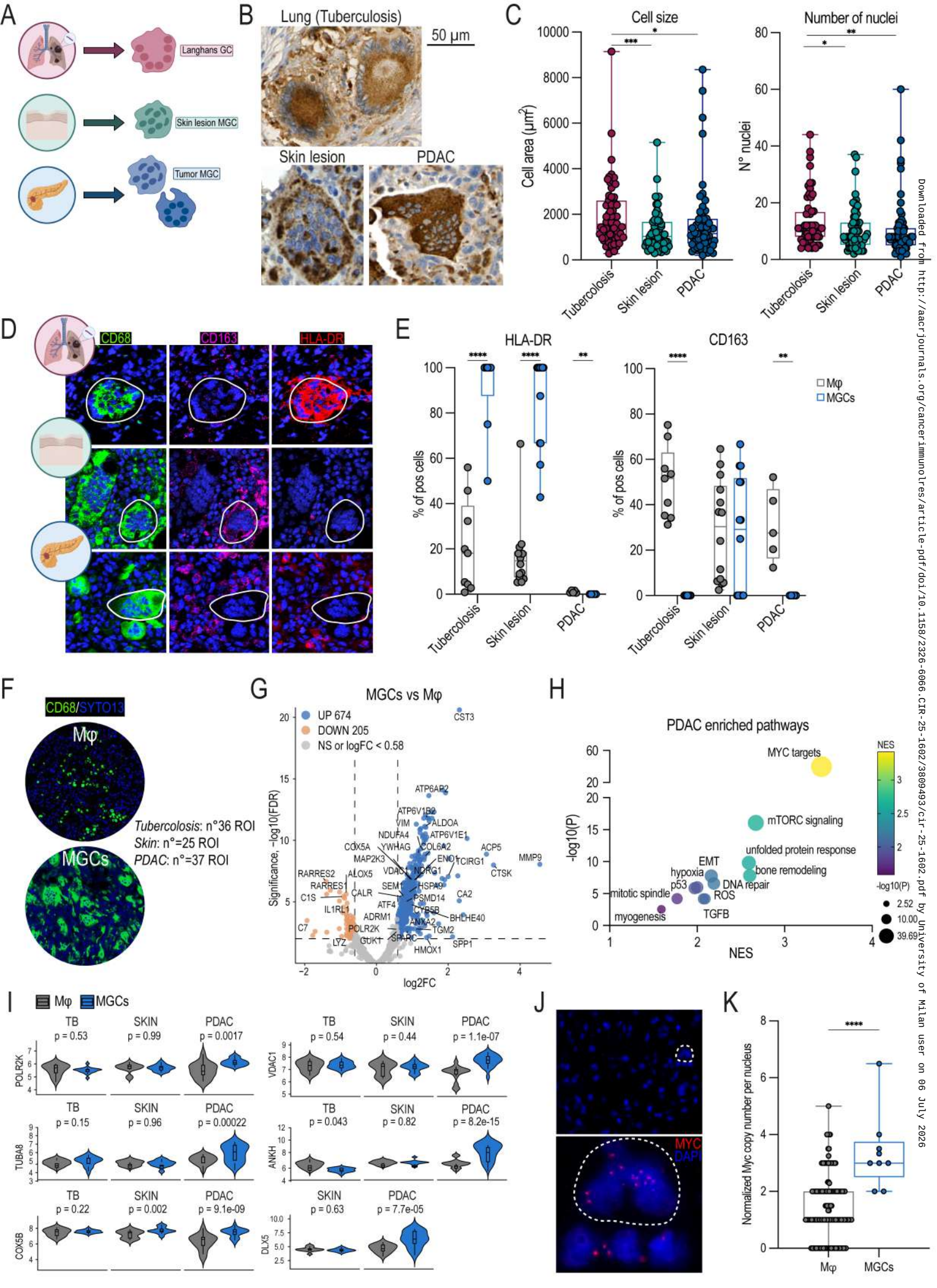

Figure 2

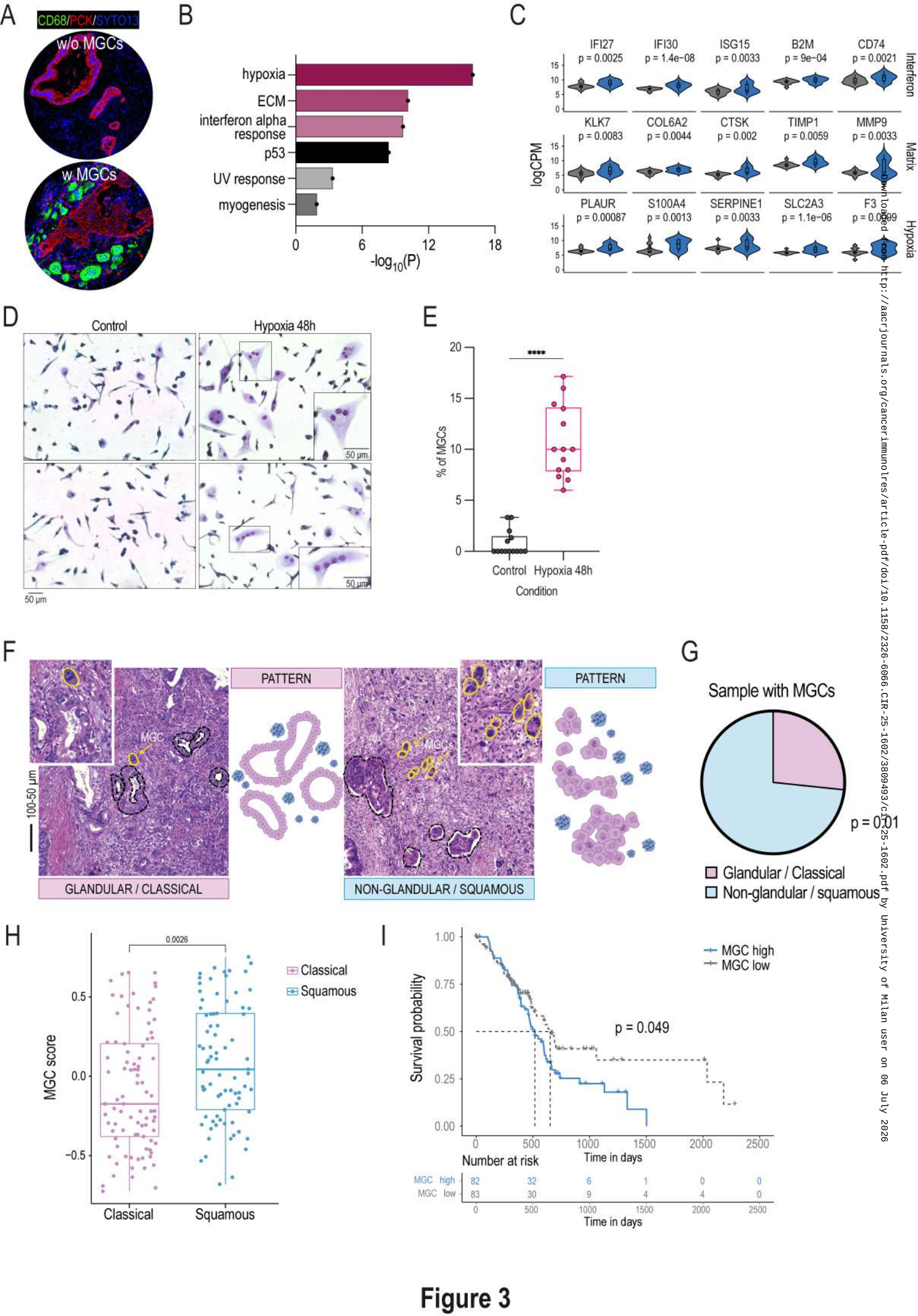

Figure 3

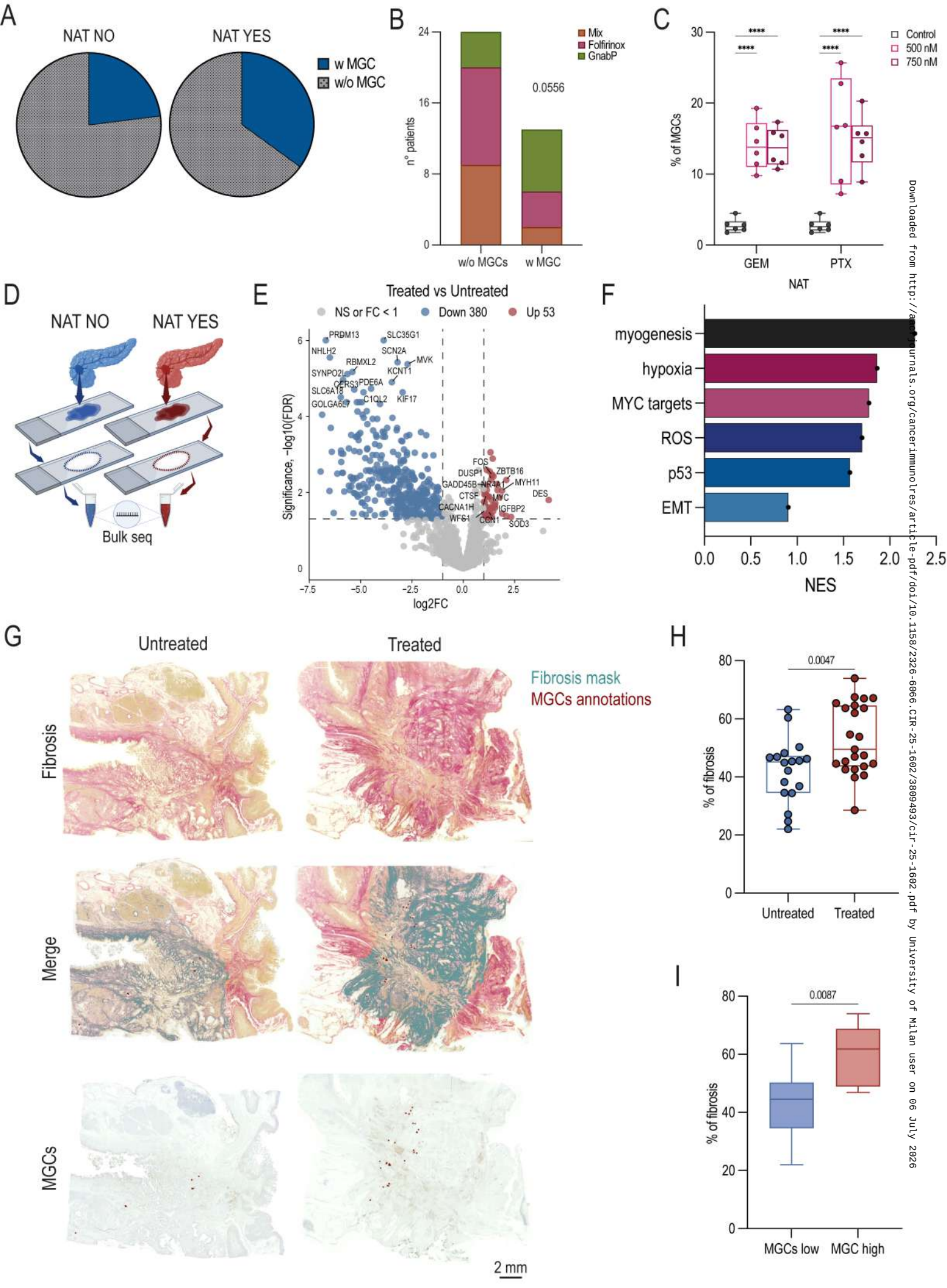

Figure 4

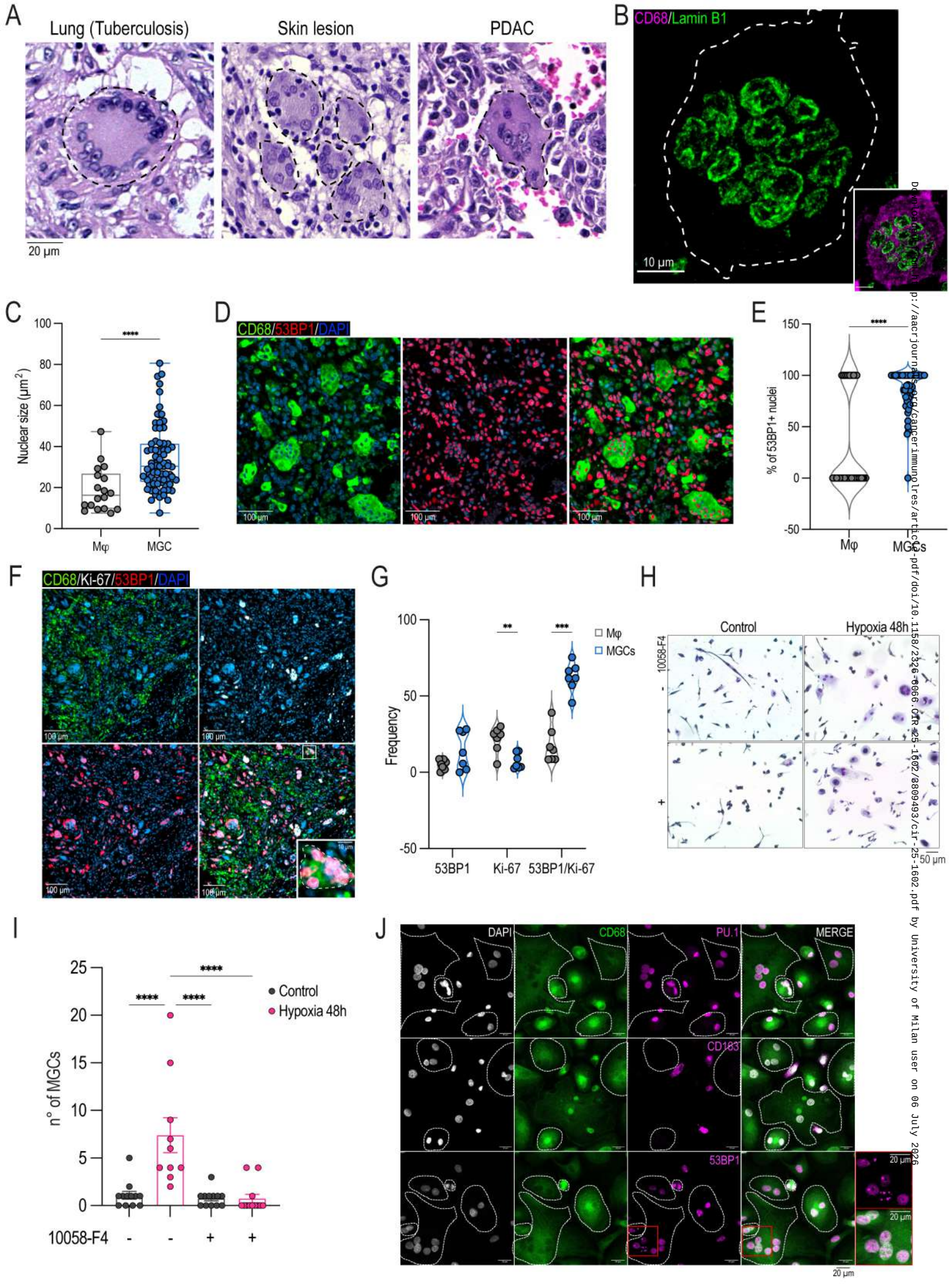

Figure 5